

Real-Time Incremental Explanations for Object Detectors in Autonomous Driving

Santiago Calderón-Peña, Hana Chockler, David A. Kelly

King's College London

London, United Kingdom

{santiago.calderon, hana.chockler, david.a.kelly}@kcl.ac.uk

Abstract

Object detectors are widely used in safety-critical real-time applications such as autonomous driving. Explainability is especially important for safety-critical applications, and due to the variety of object detectors and their often proprietary nature, black-box explainability tools are needed. However, existing black-box explainability tools for AI models rely on multiple model calls, rendering them impractical for real-time use.

In this paper, we introduce INCX, an algorithm and a tool for real-time black-box explainability for object detectors. The algorithm is based on linear transformations of saliency maps, producing sufficient explanations. We evaluate our implementation on four widely used video datasets of autonomous driving and demonstrate that INCX's explanations are comparable in quality to the state-of-the-art and are computed two orders of magnitude faster than the state-of-the-art, making them usable in real time.

1. Introduction

AI models are now a primary building block of most computer vision systems. However, the inherent opacity of some of these models (e.g., neural networks) and their sharp increase in size and complexity, slow their adoption, especially in safety-critical applications, due to the need to understand the reasoning of the model [2].

Explainable AI (XAI) is used to provide insights into the decision-making process of machine learning models. Post hoc XAI can be roughly divided into “white-box” and “black-box” methods. White-box methods have access to the internals of the model, and are hence tailored to a particular model architecture. Black-box methods can only access model outputs and are agnostic to the internal implementation of the model. In this paper we focus on black-box explainability, due to its portability across models.

Explainable AI is particularly relevant in the context of

autonomous driving, as it is instrumental in assessing safety of autonomous vehicles. Regulatory bodies can greatly benefit from XAI by improving model explainability, which aids in product liability litigation and compliance assessments [10]. Furthermore, industry standards for road vehicle safety, such as ISO21448 [21], emphasize the need for traceability of performance insufficiencies and their trigger conditions. In this regard, explainable AI has been proposed as a means of enhancing implementation transparency, contributing to the development of inherently safe AI systems in autonomous driving (AD) [31].

Object detection is crucial in AD for various tasks, including traffic sign and light recognition [24]. Visual explanations, such as saliency maps, are essential for enhancing transparency and trust in autonomous driving systems [3]. They aid in generating textual observations and improving system interpretability [25]. Explaining object detectors, however, is challenging. On the one hand, most AD approaches rely on white-box algorithms [5, 33], which are primarily based on gradient propagation, restricting their applicability to specific architectures. On the other hand, while black-box methods are model-agnostic, their high computational cost makes real-time explanations infeasible [32].

To enhance autonomous driving models’ explainability, we introduce *Incremental eXplanations*, or INCX —a black-box XAI algorithm and tool for explaining object detectors in real-time. INCX avoids multiple calls to the model and thus has a negligible overhead over the object classification running time, allowing near real-time explanation processing for video data. INCX tracks saliency maps from one frame to the next, applying linear transformations to the saliency map generated in the first frame, and uses these maps to compute sufficient explanations—subsets of pixels of the image sufficient for the original classification. Unlike FastSHAP [22], it does not rely on a separate machine learning model that would necessitate, in turn, its own explanations.

We show that INCX computes explanations that are com-

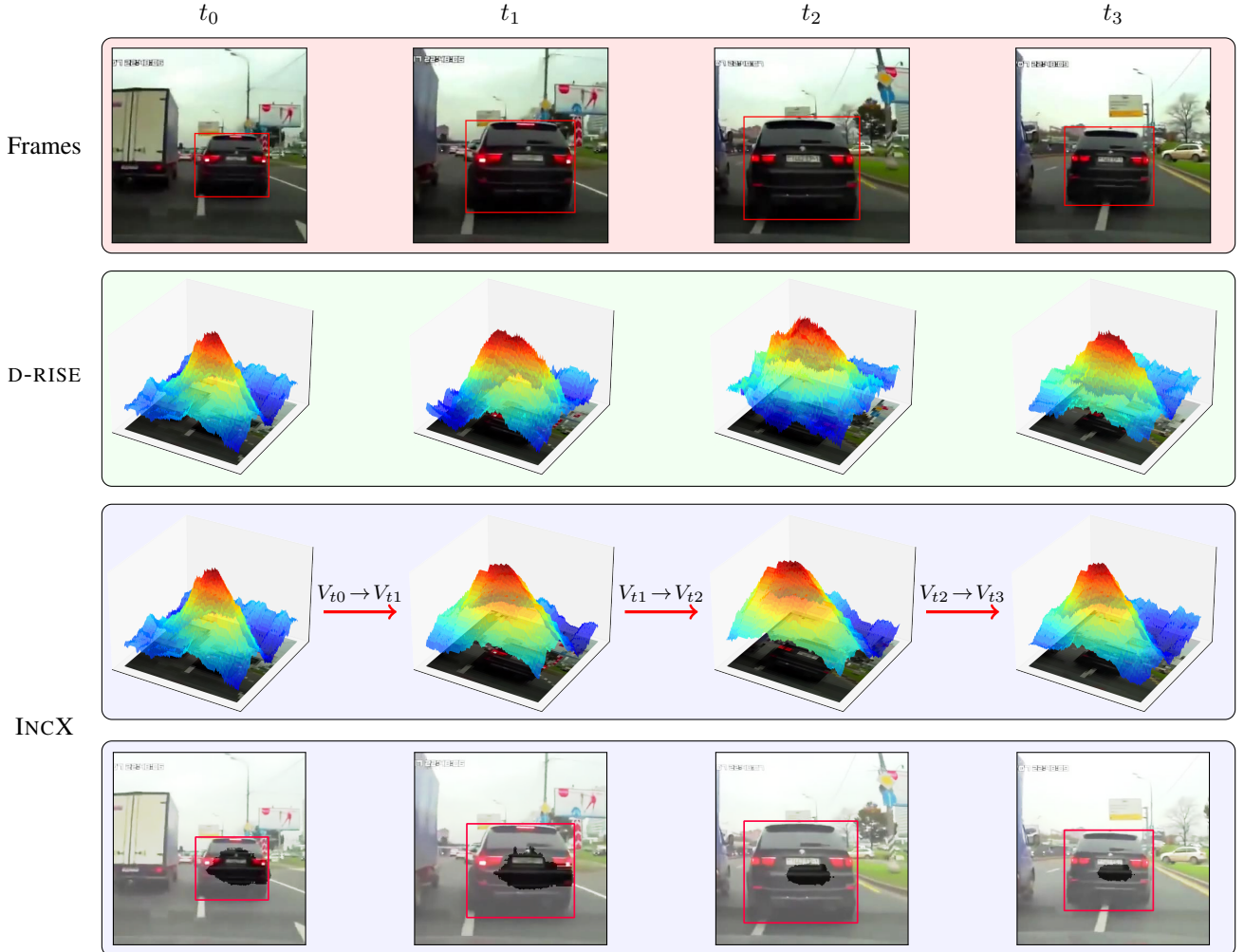


Figure 1. Detection of an object ‘car’ (Frames) at four different time stamps, with D-RISE saliency landscapes and the approximate landscapes generated by INCX, showing the similarity between the fully computed D-RISE saliency maps and the estimated INCX ones. V_t represents the object at time t .

parable in quality to D-RISE [36], but outperforms D-RISE in speed by two orders of magnitude. To the best of our knowledge, this is the first black-box real-time XAI tool for object detectors.

The code, the benchmark sets, full proofs, and the full tables of results are submitted as a part of the supplementary material. Instructions for running INCX locally in a docker container and seeing the explanations in real time are also provided.

2. Related Work

We survey the related work in object detection, tracking, and explainability. Since this work focuses on black-box explainability, we do not include white-box XAI methods, such as GradCAM [41] or DexT [34].

Explainability for image classifiers There is a large body of work on explainability for image classifiers. Common black-box tools are LIME [39], SHAP [30], RISE [35], and ReX [9]. These tools and algorithms define and output explanations in different formats: functions, models and landscapes. There is a straightforward conversion of different formats of explanations to *saliency maps*, which rank input pixels based on their contribution to the model classification. Black-box tools generally rely on multiple calls to the model, computing explanations from these results, and hence incurring a significant overhead on top of the image classifier.

Object detection in AD The object detection task is finding objects and classifying them under low latency. This capability is fundamental in autonomous driving, as it en-

ables the vehicle to recognize other automobiles and traffic signs in real time.

YOLO [37], a collection of one-stage algorithms, has enjoyed a considerable popularity due to its balance between efficiency and accuracy, leading to adoption in autonomous driving research [1]. It divides the image into a grid of cells and assigns a set of class probabilities, a bounding box, and a confidence value. Then it performs non-maximum suppression to remove overlapping bounding boxes. The latest version, 10th as of time of writing, addresses many of the shortcomings of the original YOLO [43].

In contrast, a two-stage process uses a region proposal network (RPN) to identify regions within the image that contain an object. Then it takes those regions and warps them into a classifier network to find the probabilities of the objects inside the image. Examples of such architectures include Faster R-CNN [38], R-CNN [18] and Fast R-CNN [17]. This approach has also been extensively used in AD research [28].

Transformer-based detectors have been popular since the introduction of the transformer architecture, which revolutionized the Natural Language Processing (NLP) domain, as it introduced the self-attention mechanism [42]. The Real-Time Detection Transformer (RT-DETR) leverages the same concept for object detection tasks [49].

Explainability for object detectors Several XAI algorithms can be modified to provide explainability for object detectors. There are only a few black-box algorithms that generate saliency maps without relying on the model architecture. D-RISE [36] is a modification of RISE for black-box object detectors, using the basic underlying idea of RISE to generate a set of random masks. D-RISE also introduces the concept of a detection vector, composed of localization information (bounding boxes), object score, and classification information. It then uses this vector to compute a weight for each mask and construct a saliency map given by the weighted sum of masks. In contrast, FSOD [26] adapts the loss function of FastSHAP to train an explainer model with an architecture inspired by UNet to account for classification and location of the detected object [23]. Although this approach exhibits a considerably faster performance than the previously mentioned ones, its major drawback is that it lacks explainability for the explainer model itself.

Multiple Object tracking (MOT) Detection-based tracking (DBT) is the dominant paradigm in multiple object tracking tasks. These methods divide the tracking sub-problem into three main tasks: object detection, re-identification (ReID) and trajectory tracking [12]. A classic example of a Multi-object tracker within this paradigm is SORT [4], which is the algorithm we use in this paper. SORT uses a Kalman filter to perform estimations of

previously detected objects. Subsequently, it associates the identified objects via the Intersection over Union (IoU) of the bounding box of the detected object and the estimated position and scale of the bounding box. It uses the Hungarian algorithm to optimally solve this assignment. There is a number of algorithms implementing improvements to SORT, such as DeepSORT [46], StrongSORT [13], and ByteTrack [48], but these rely on an additional deep learning model, detracting from transparency.

Explainable AI in Autonomous Driving Explainable AI for safe autonomous driving can be categorized into several approaches [27]. Interpretable by design models are inherently transparent, such as traffic sign detectors built with Inductive Logic Programming [7]. Interpretable surrogate models approximate black-box behavior with explainable alternatives like LIME [39]. Interpretable monitoring employs saliency maps to track model behavior and detect anomalies [19]. Interpretable validation ensures reliability through offline interpretable methods. Together, these techniques strengthen AI transparency and safety in autonomous driving.

3. Incremental Explanations

In this section we present our contribution – the INCX algorithm. Full proofs of all theorems and lemmas are provided in the supplementary material.

3.1. Theoretical Foundations

The intuition behind our algorithm is based on the following lemma.

Lemma 1. *For a fixed observer, movement of an object in 3D space without rotation or deformation can only result in a combination of scaling and linear translation when projected on a given vertical plane.*

Proof Sketch. The lemma follows from the observation that the vector of movement of an observed object is a sum of its projections to the vertical plane and in the direction to or away from the observer. The vector to or away from the observer determines the scaling, while the projection to the vertical plane determines the linear translation. \square

Given a transformation of the observed object as above and its initial saliency map, we prove that the saliency map of the transformed object can be computed from the original saliency map using a similar transformation.

The main result is stated in Theorem 1. The formal proof is based on results from probability theory and is quite involved (see the supplementary material). Before presenting the theorem, we first introduce additional context and formalization to ensure a clearer understanding.

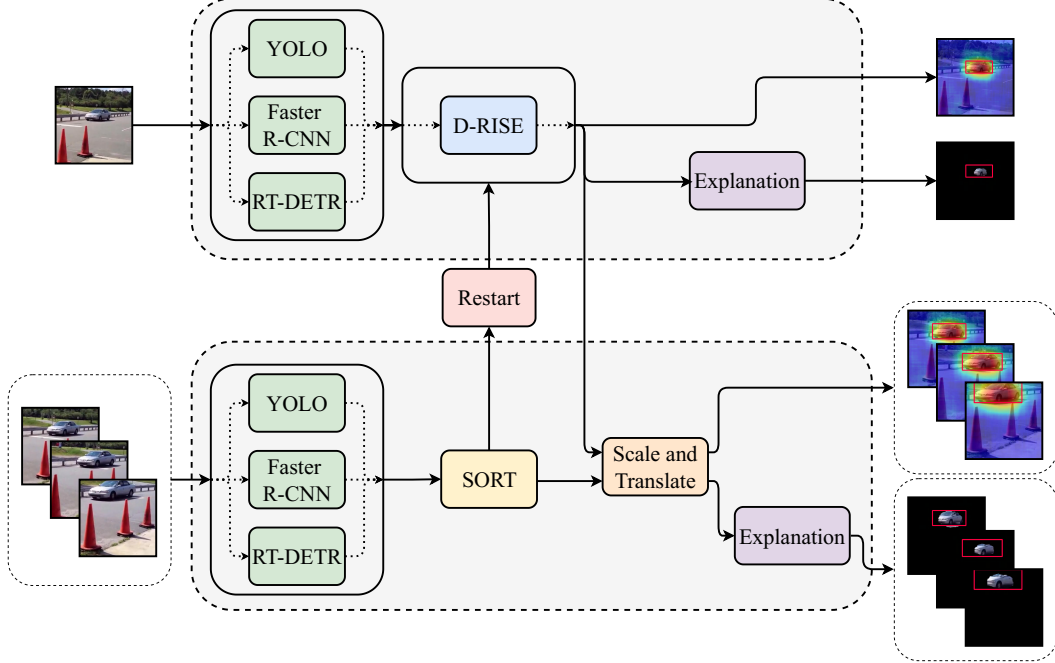


Figure 2. Block diagram of INCX components: First frame process (Top) and subsequent frames (Bottom)

Intuitively, the proof is based on converting the saliency map to a *probability mass function (pmf)* and then applying the mathematics of pmf transformation to estimate a pmf for a new, updated, saliency map.

First, the initial saliency map is converted into a pmf by normalizing the values of the saliency map. Then we use Lemma 2 [20] to define the transformations of the pmf. This allows us to calculate the new saliency pmf after undergoing linear transformation. Technically, our pmf is a joint probability mass function $P(X, Y)$. We restate the core transformation result over a single variable from Hogg et al. [20] here for completeness.

Lemma 2 ([20]). *Assume X to be a discrete random variable with space D_X and g a one-to-one transformation function. Then the space of Y is $D_Y = \{g(x) : x \in D_X\}$, and the pmf of Y is*

$$p_Y(y) = P[g(X) = y] = P[X = g^{-1}(y)] = p_X(g^{-1}(y)).$$

Lemma 2 can be extended to joint pmfs over multiple variables [20, p.100] (see supplementary material).

Having established the intuition behind the transformation of the saliency pmf, we address the considerations of our approach concerning transformations involving three-dimensional objects. Specifically, we first describe how such objects get projected onto the image plane. By Forsyth and Ponce [15], the mapping of points from three-dimensional world coordinates to two-dimensional

screen coordinates can be achieved while using a common frame of reference for the world and the camera. Lemma 3 formalizes this projection process.

Lemma 3. *Let $\alpha, \beta \in \mathbb{R}$ denote the intrinsic magnification factors of the camera. The transformation from 3D world coordinates (x, y, z) to 2D screen coordinates (u, v) is given by:*

$$\begin{bmatrix} u \\ v \end{bmatrix} = \frac{1}{z} \begin{bmatrix} \alpha & 0 & O_x \\ 0 & \beta & O_y \end{bmatrix} \begin{bmatrix} x \\ y \\ z \end{bmatrix} = \frac{1}{z} \mathcal{K} \begin{bmatrix} x \\ y \\ z \end{bmatrix}$$

where \mathcal{K} represents the intrinsic parameters of the camera, and (O_x, O_y) represents the coordinates at the upper-left corner of the image.

We formalize the intuition of a *center* of a bounding box for the projected object in Definition 1. This concept is leveraged in the scaling and translation operations described in Definition 2, which are fundamental for INCX.

Definition 1 (Center Function). *The center function $\mathbf{C} : 2^{\mathbb{R}^n} \rightarrow \mathbb{R}^n$ maps a set $S \subset \mathbb{R}^n$ of points to the center point of the bounding box that encloses these points. For a set S consisting of points $\mathbf{p} = (p_1, p_2, \dots, p_n) \in \mathbb{R}^n$ the function is defined as follows:*

$$\mathbf{C}(S) = \begin{bmatrix} \frac{\max(p_1) + \min(p_1)}{2} \\ \frac{\max(p_2) + \min(p_2)}{2} \\ \vdots \\ \frac{\max(p_n) + \min(p_n)}{2} \end{bmatrix}$$

where $\max(p_j)$ and $\min(p_j)$ denote the maximum and minimum values, respectively, of the j -th coordinate among all points in S .

Definition 2 (Scaling and Translation). Let $A = \{(u, v) \in \mathbb{R}^2\}$ represent a set of points defining an area in the image space.

Scaling is a linear transformation $S : \mathbb{R}^2 \rightarrow \mathbb{R}^2$, defined as $S(\mathbf{p}) = \gamma(\mathbf{p} - \mathbf{C}(A))$, where $\mathbf{p} \in A$ and $\gamma \in \mathbb{R}^{2 \times 2}$ is a diagonal matrix.

Translation is a linear transformation $T : \mathbb{R}^2 \rightarrow \mathbb{R}^2$, defined as $T(\mathbf{p}) = \mathbf{p} + \mu$, where $\mathbf{p} \in A$.

The scaling transformation S modifies a point \mathbf{p} by a factor of γ , after first shifting it relative to the center of the area of the object in the image. Specifically, applying S to all points in A is equivalent to scaling the entire image while moving the center of mass $\mathbf{C}(A)$ to the origin $(0, 0)$. The translation function T shifts the two-dimensional point \mathbf{p} by a vector $\mu \in \mathbb{R}^2$. Similarly, applying this transformation to all points in an image results in translating the entire image by μ .

We first provide the intuition behind our theorem and then its formal statement in Theorem 1. Our approach maps a given pmf to a 2D-projection of a three-dimensional object δ_t (see Assumption 1). Furthermore, as long as the object being tracked does not leave the frame, rotate, or is occluded by another object, the future positions of the object are determined solely by translation and scaling transformations in the three-dimensional space (see Assumption 2). Together, these assumptions lead to the statement that future saliency maps can be computed by applying a scaling and translation linear transformation to the current saliency map.

We use the following notation. Let $\mathbf{Q}_t = (Q_{1,t}, Q_{2,t})$ be a vector in the image space at time t , where $Q_{1,t}$ and $Q_{2,t}$ represent random variables along the u -axis and the v -axis, respectively. The pmf of \mathbf{Q}_t is $p_{\mathbf{Q}_t}(\mathbf{q}_t)$, which is derived from the normalized saliency map.

We assume that the expected value of the saliency pmf, if it exists, is equal to the center of the bounding box $\mathbf{C}(\mathcal{K}V_t)$ of the object V_t as projected into the image space using the matrix \mathcal{K} . δ_t represents the distance between this projected center and the expected value of \mathbf{Q}_t . The main reason behind this assumption is the homogeneity of our pmf, implying that any scaling or translation of the expected value results in a corresponding scale or shift of the entire pmf,

preserving the distribution's proportions. A direct implication of this assumption is that if we move and scale the center of the bounding box, then the saliency map would have a similar shift and scaling.

Assumption 1 (Expected Value and Bounding Box Center Relation).

$$\mathbb{E}[\mathbf{Q}_t] = \mathbf{C}(\mathcal{K}V_t) + \delta_t$$

Assumption 2 (Constrained Affine Transformation). Any point of an object at time $t + 1$ is related to the same object at time t by an affine transformation given by:

$$\begin{bmatrix} x_{t+1} \\ y_{t+1} \\ z_{t+1} \\ 1 \end{bmatrix} = \begin{bmatrix} m_x & 0 & 0 & 0 \\ 0 & m_y & 0 & 0 \\ 0 & 0 & m_z & 0 \\ 0 & 0 & 0 & 1 \end{bmatrix} \begin{bmatrix} \mathbf{I} & \mathbf{t} \\ \mathbf{0}^T & 1 \end{bmatrix} \begin{bmatrix} x_t \\ y_t \\ z_t \\ 1 \end{bmatrix}$$

where $\mathbf{t} \in \mathbb{R}^3$ is a translation vector, $\mathbf{I} \in \mathbb{R}^{3 \times 3}$ is the identity matrix, and m_x, m_y , and $m_z \in \mathbb{R}$ are scaling factors.

Finally, let S be the scaling function, T the translation function, \mathbf{q}_{t+1} a coordinate vector in the image space at time $t + 1$, and \mathbf{q}_t a coordinate vector at time t . The following theorem describes the relation between the pmf at time t and at time $t + 1$ and is instrumental to our algorithm.

Theorem 1. If Assumptions 1 and 2 hold, then the pmf at time $t + 1$, $p_{\mathbf{Q}_{t+1}}(\mathbf{q}_{t+1})$, can be computed from the pmf at time t using the following equation:

$$p_{\mathbf{Q}_{t+1}}(\mathbf{q}_{t+1}) = p_{\mathbf{Q}_t}(S^{-1}(T^{-1}(\mathbf{q}_{t+1})))$$

3.2. Algorithm Structure

The INCX algorithm is schematically presented in Figure 2, and its pseudo-code is shown in Algorithm 1. In Figure 2, we list the object detectors used for the experiments in the paper, however INCX is agnostic to the detector, hence any object detector can be plugged in.

The saliency map in the first frame is computed using an XAI tool (in our experiments we used D-RISE). The *Explanation* procedure is used to extract a sufficient explanation from the saliency map (see Section 3.3 below). After this bootstrapping, INCX computes saliency maps and sufficient explanations for subsequent frames by performing the transformation described in Theorem 1 on the output of the previous frames.

As shown in Algorithm 1, in subsequent frames INCX maps the current objects to the objects that are tracked in the previous frame using SORT [4]. Once the mapping is computed, the algorithm computes the linear transformation of the bounding boxes of the mapped objects by calling the Transform function (Line 8). This transformation is applied to the saliency map of the previous frame, using Theorem 1.

Algorithm 1 Pseudo-code of INCX

Input: Video v , object detector \mathcal{N} , explainer h , tracker SORT

Output: List of explanations xp and estimated saliency maps s

```

1: initialize bounding boxes and saliency map
2: initialize empty saliency list  $s$  and explanation list  $xp$ 
3: for each frame  $f_t$  at time  $t$  in  $v$  do
4:    $(x_t, y_t, w_t, h_t) \leftarrow \mathcal{N}(f_t)$ 
5:   if  $t = 0$  then
6:      $s_t \leftarrow h(f_t)$  {Initial saliency map}
7:   else
8:      $s_t \leftarrow \text{Transform}(s_{t-1})$  {track object(s) from previous frame}
9:   end if
10:   $xp_t \leftarrow \text{Explanation}(s_t, \mathcal{N}, f_t, t)$ 
11:   $xp \leftarrow xy \cup xp_t$ 
12:   $s \leftarrow s \cup s_t$ 
13: end for
14: return  $xp, s$ 

```

Note that if the new saliency map is scaled up, the gaps in the new pmf are filled using interpolation.

The algorithm can compute explanations only for objects detected by the object tracker. An object might leave the frame or remain undetected for a period of time and reappear later. For efficiency, we define a *timeout* that allows us to stop attempting to explain an object, which is no longer detectable.

3.3. Sufficient explanations

Thus far, we have discussed saliency maps. It is also useful to provide *sufficient* explanations. We use the following definition, which is a standard definition of causal explanations for image classifiers [8].

Definition 3 ([8]). *An explanation is a minimal subset of pixels of a given input image that is sufficient for the model to correctly detect the object, with all other pixels of the image set to a baseline value (occluded).*

Computing minimal and sufficient explanations is intractable [8], so we relax the minimality requirement. A *sufficient explanation* is a subset of pixels of the input image that is sufficient for the AI model to reproduce the original classification of the entire image. This is a useful sanity check of the saliency maps: the “hot spots” on the saliency map should be sufficient to trigger the original object detection. Sufficient explanations are computed by the *Explanation* procedure for both the initial and the subsequent frames, as shown in Figure 2. We note that, while the saliency maps for subsequent frames are approximate, the extracted explanations are still correct, that is, sufficient

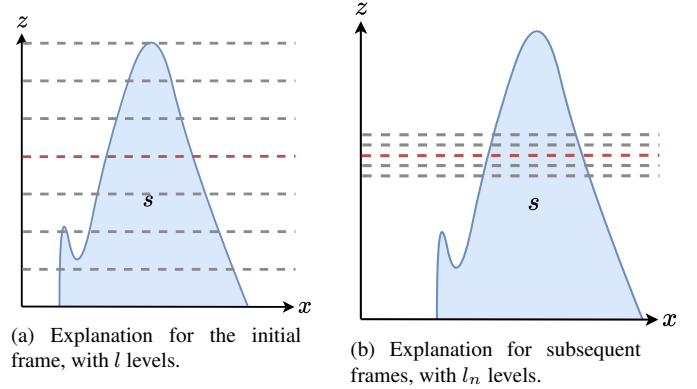


Figure 3. Visualization of the *Explanation* procedure.

for the original classification. They can, however, be larger than those computed from baseline saliency maps.

A brute-force extraction of sufficient explanations from saliency maps is inefficient, as it requires checking all subsets of pixels of the image. Our *Explanation* procedure, illustrated in Figure 3b (see also the pseudo-code in the supplementary material) uses a binary search on the saliency map of the current frame, as described below.

For the initial frame, the saliency map is divided into l equal horizontal sections, as illustrated in Figure 3a (lateral view). The goal is to determine the smallest region that is sufficient for the model to make the same prediction. Therefore, we progressively occlude the pixels under a given dotted line. We then query the model with the partially occluded input to check whether the object is still being detected.

A naive approach would require querying the model at every possible dotted line, which is computationally expensive. Instead, we use binary search to efficiently locate a threshold (depicted by the red dotted line) that provides a sufficient, albeit not necessarily minimal, explanation. This approach works because the property of being sufficient is monotonic. In other words, starting from the top of the saliency map, as we reveal more of the image, the explanation becomes sufficient at some point and stays sufficient for all subsequent values.

Explanation discovery for subsequent frames is depicted in Figure 3b. Assuming temporal consistency in the saliency map, it is reasonable to expect that the explanation threshold in subsequent frames will be close to that of the previous frames. Therefore, we start our binary search around the previous threshold, with the number of divisions adjusted to a parameter l_n . Smaller values of l_n improve performance but may result in explanations that contain more redundancy.

Dataset	Model	Explainer	Ins. (↑)	Del. (↓)	EPG (↑)	EP (↓)	Time(s) (↓)
BDD100K	Faster R-CNN	D-RISE	0.9459	0.0233	0.1974	0.0125	170.55
		IncX	0.9448	0.0246	0.2009	0.0151	1.06
	RT-DETR	D-RISE	0.9321	0.0510	0.2542	0.0387	130.30
		IncX	0.9312	0.0478	0.2658	0.0304	2.54
	YOLO	D-RISE	0.7879	0.0326	0.2771	0.0816	44.83
		IncX	0.8109	0.0354	0.3159	0.0700	1.22
KITTI	Faster R-CNN	D-RISE	0.9705	0.0212	0.0968	0.0070	129.06
		IncX	0.9646	0.0214	0.1384	0.0074	2.15
	RT-DETR	D-RISE	0.9741	0.0139	0.0818	0.0114	114.09
		IncX	0.9760	0.0157	0.1071	0.0131	4.23
	YOLO	D-RISE	0.9031	0.0153	0.1197	0.0485	40.32
		IncX	0.8970	0.0158	0.1330	0.0521	2.60
NuScenes	Faster R-CNN	D-RISE	0.9827	0.0035	0.0322	0.0089	203.56
		IncX	0.9771	0.0034	0.0366	0.0118	23.25
	RT-DETR	D-RISE	0.9119	0.0304	0.1199	0.0293	225.65
		IncX	0.9011	0.1182	0.1201	0.0272	38.84
	YOLO	D-RISE	0.7639	0.0117	0.1212	0.0813	95.45
		IncX	0.7777	0.0132	0.1202	0.1178	14.37
VIPER	Faster R-CNN	D-RISE	0.9417	0.0452	0.1705	0.0177	277.44
		IncX	0.9368	0.0641	0.1502	0.0094	22.91
	RT-DETR	D-RISE	0.9465	0.1420	0.3373	0.0617	245.32
		IncX	0.9388	0.1304	0.4059	0.0777	27.91
	YOLO	D-RISE	0.7128	0.0555	0.3284	0.1280	114.30
		IncX	0.7482	0.0599	0.4406	0.1154	9.80

Table 1. Comparison of different models across multiple datasets using D-RISE and INCX as explainers. The arrows indicate whether higher (↑) or lower (↓) values of each metric are better.

4. Experimental Results

The COCO [29] and VOC [14] datasets are typically used for evaluation of explainability in object detection [26]. However, these datasets consist of independent images that lack temporal continuity, making them unsuitable for our focus on real-time video explanation for autonomous vehicles. To address this limitation, we selected datasets specifically designed for autonomous driving, namely BDD100K [47], KITTI [16], NuScenes [6] and VIPER [40], each of which contain hundreds of thousands of individual frames distributed across hundreds of videos. Given the computational expense of explanation methods such as D-RISE, processing these datasets in full would be impractical. To ensure feasible benchmarking, we randomly selected a representative subset from each dataset. From KITTI, BDD100K, and VIPER, we chose

five videos each and extracted 100 frames per video. For KITTI, this corresponds to 10 seconds per video at 10 FPS. For NuScenes, we used the entire mini dataset, consisting of 10 videos of 404 frames.

We evaluated INCX on the following object detectors: YOLOv10-n, RT-DETR-l, and the PyTorch implementation of Faster R-CNN. D-RISE was used to compute the initial saliency maps. INCX makes no assumptions about how the initial saliency map is produced: D-RISE is used as it works naturally with the different object detectors that we examine and is considered the state-of-the-art explainability tool for object detectors. For comparison we also computed the saliency maps independently using D-RISE for all frames. We executed D-RISE with 1000 mutants and a mask resolution of (4, 4). All experiments were conducted using the NVIDIA A100 Tensor Core GPU.

Dataset	Model	CC	SSIM
BDD100K	Faster R-CNN	0.9395	0.8599
	RT-DETR	0.9648	0.8383
	YOLO	0.9307	0.7447
KITTI	Faster R-CNN	0.9071	0.5832
	RT-DETR	0.9118	0.5625
	YOLO	0.9308	0.7471
NUSCENES	Faster R-CNN	0.9433	0.8284
	RT-DETR	0.9028	0.8023
	YOLO	0.9221	0.8494
VIPER	Faster R-CNN	0.9147	0.8308
	RT-DETR	0.8661	0.7124
	YOLO	0.8203	0.6464

Table 2. Correlation Coefficient (CC) and Structural Similarity Index Measure (SSIM) scores used for comparing saliency maps across different models for each dataset.

Dataset	Model	JI	DC
BDD100K	Faster R-CNN	0.3308	0.4371
	RT-DETR	0.5582	0.6611
	YOLO	0.6660	0.7853
KITTI	Faster R-CNN	0.4323	0.5535
	RT-DETR	0.5655	0.6996
	YOLO	0.6861	0.7993
NUSCENES	Faster R-CNN	0.5603	0.6774
	RT-DETR	0.5387	0.6325
	YOLO	0.7144	0.7967
VIPER	Faster R-CNN	0.4220	0.5055
	RT-DETR	0.4252	0.5466
	YOLO	0.6147	0.7380

Table 3. Jaccard Index (JI) and Dice Coefficient (DC) scores used for comparing explanations across different models for each dataset.

For a one-to-one comparison between each saliency map generated by D-RISE and INCX, we computed a set of metrics commonly used in the field of Explainable AI. We describe these metrics below.

The **Normalized Insertion/Deletion curves** metric starts with a blank image, adding pixels based on the saliency map, and computes the area under the curve (AUC) after measuring detector confidence. Conversely, the deletion process starts with the full image and gradually removes pixels according to the saliency map. For object detectors, we adjust this metric by multiplying the score by the Intersection over Union (IoU) of the original bounding box. This adjustment accounts for the fact that traditional insertion and deletion curves assess whether an object is detected, but do not consider its precise location, an essential factor for object detection tasks. To account for low confi-

dence producing low insertion and deletion values, we normalize the curve by dividing all values by the original image’s softmax classification.

The **Energy-based Pointing Game (EPG)** metric quantifies the proportion of the saliency map’s total energy that is contained within the bounding box [44]. This metric is essential because an accurate saliency map should predominantly cover the bounding box to correctly represent the object of interest. If the saliency map is focused outside of the bounding box, it may indicate the detection of an object that does not correspond to the one within the current bounding box.

The **Explanation Proportion (EP)** metric measures explanation quality by computing the ratio of the explanation to the whole image, hence favoring compact explanations that minimize unnecessary information. We define EP as follows: for a given boolean-valued mask m of an image, where \top denotes the pixels included in the explanation, the EP is computed as

$$EP = \frac{\sum_{(i,j) \in \top} m_{(i,j)}}{\sum_{(i,j) \in \top} m_{(i,j)} + \sum_{(i,j) \notin \top} m_{(i,j)}} \quad (1)$$

As summarized in Table 1, the insertion values for INCX are consistently within 5% of those observed for D-RISE, with all other metrics displaying similar trends. Moreover, the running time of INCX is two orders of magnitude less than that of D-RISE in most cases, showing that INCX is suitable for real-time scenarios.

The quality of an approximate saliency map computed by INCX is evaluated by measuring its deviation it from the baseline saliency map, computed by D-RISE directly from the image. We compute this deviation by using standard metrics: Pearson Correlation Coefficient (CC), Structural Similarity Index (SSIM) [45] (Table 2), Dice Coefficient (DC) [11], and Jaccard Index (IoU) (Table 3). The results in both tables indicate a strong similarity between the saliency maps generated by INCX and the baseline maps produced by D-RISE.

Limitations INCX assumes that the object it is applied to is rigid and does not rotate. Our experimental results show that this assumption is reasonable in practice for autonomous driving. Another implicit assumption is that consecutive frames produce similar saliency maps, which is supported by the laws of physics: objects tend not to disappear or (re-)materialize.

5. Conclusions

In this paper we have presented the algorithm INCX for real-time explanations of object detectors. The algorithm incurs a negligible overhead on the object detector and is two orders of magnitude faster than the state-of-the-art. Our

method does not lead to inferior quality saliency maps, despite its assumptions. The standard quality metrics for assessing XAI algorithms show that INCX is comparable to D-RISE, the state-of-the-art in black-box XAI for object detectors. Evaluation across multiple standard datasets supports our claim that INCX is suitable for autonomous driving applications.

References

- [1] Nusaybah M. Alahdal, Felwa Abukhodair, Leila Haj Meftah, and Asma Cherif. Real-time object detection in autonomous vehicles with yolo. *Procedia Computer Science*, 246:2792–2801, 2024. 28th International Conference on Knowledge Based and Intelligent information and Engineering Systems (KES 2024). [3](#)
- [2] Ananthaswamy Anil. In AI, is bigger better? *Nature*, pages 202–225, 2023. [1](#)
- [3] Shahin Atakishiyev, Mohammad Salameh, Hengshuai Yao, and Randy Goebel. Explainable artificial intelligence for autonomous driving: A comprehensive overview and field guide for future research directions. *IEEE Access*, 2024. [1](#)
- [4] Alex Bewley, Zongyuan Ge, Lionel Ott, Fabio Ramos, and Ben Upcroft. Simple online and realtime tracking. In *2016 IEEE International Conference on Image Processing (ICIP)*, pages 3464–3468, 2016. [3, 5](#)
- [5] Mariusz Bojarski, Anna Choromanska, Krzysztof Choromanski, Bernhard Firner, Larry J Ackel, Urs Muller, Phil Yeres, and Karol Zieba. Visualbackprop: Efficient visualization of cnns for autonomous driving. In *2018 IEEE International Conference on Robotics and Automation (ICRA)*, pages 4701–4708, 2018. [1](#)
- [6] Holger Caesar, Varun Bankiti, Alex H. Lang, Sourabh Vora, Venice Erin Liang, Qiang Xu, Anush Krishnan, Yu Pan, Giancarlo Baldan, and Oscar Beijbom. nuScenes: A Multimodal Dataset for Autonomous Driving . In *2020 IEEE/CVF Conference on Computer Vision and Pattern Recognition (CVPR)*, pages 11618–11628, Los Alamitos, CA, USA, 2020. IEEE Computer Society. [7](#)
- [7] Zahra Chaghazardi, Saber Fallah, and Alireza Tamaddoni-Nezhad. Explainable and trustworthy traffic sign detection for safe autonomous driving: An inductive logic programming approach. In Proceedings 39th International Conference on Logic Programming, Imperial College London, UK, 9th July 2023 - 15th July 2023, pages 201–212. Open Publishing Association, 2023. [3](#)
- [8] Hana Chockler and Joseph Y. Halpern. Explaining image classifiers, 2024. [6](#)
- [9] Hana Chockler, David A. Kelly, Daniel Kroening, and Youcheng Sun. Causal explanations for image classifiers, 2024. [2](#)
- [10] Ashley Deeks. The judicial demand for explainable artificial intelligence. *Columbia Law Review*, 119, 2019. Forthcoming. [1](#)
- [11] Lee R. Dice. Measures of the amount of ecologic association between species. *Ecology*, 26:297—302, 1945. [8](#)
- [12] Chenjie Du, Chenwei Lin, Ran Jin, Bencheng Chai,

Yingbiao Yao, and Siyu Su. Exploring the State-of-the-Art in Multi-Object Tracking: A Comprehensive Survey, Evaluation, Challenges, and Future Directions. *Multimedia Tools and Applications*, 2024. 3

[13] Yunhao Du, Zhicheng Zhao, Yang Song, Yanyun Zhao, Fei Su, Tao Gong, and Hongying Meng. Strong-SORT: Make DeepSORT Great Again. *IEEE Transactions on Multimedia*, 25:8725–8737, 2023. 3

[14] Mark Everingham, Luc Van Gool, Christopher KI Williams, John Winn, and Andrew Zisserman. The pascal visual object classes (voc) challenge. *International Journal of Computer Vision*, 88:303–338, 2010. 7

[15] David A. Forsyth and Jean Ponce. *Computer Vision: A Modern Approach*. Prentice Hall Professional Technical Reference, 2002. 4

[16] Andreas Geiger, Philip Lenz, Christoph Stiller, and Raquel Urtasun. Vision meets robotics: The kitti dataset. *International Journal of Robotics Research (IJRR)*, 2013. 7

[17] Ross Girshick. Fast R-CNN. In *2015 IEEE International Conference on Computer Vision (ICCV)*, pages 1440–1448, 2015. 3

[18] Ross Girshick, Jeff Donahue, Trevor Darrell, and Jitendra Malik. Rich Feature Hierarchies for Accurate Object Detection and Semantic Segmentation. In *2014 IEEE Conference on Computer Vision and Pattern Recognition*, pages 580–587, 2014. 3

[19] Lukas Hacker and Jörg Seewig. Insufficiency-driven dnn error detection in the context of sofis on traffic sign recognition use case. *IEEE Open Journal of Intelligent Transportation Systems*, 4:58–70, 2023. 3

[20] Robert Hogg, Joseph McKean, and Allen Craig. *Introduction to Mathematical Statistics*. Pearson, 2019. 4

[21] International Organization for Standardization. ISO 21448:2022 - Road vehicles — Safety of the intended functionality, 2022. 1

[22] Neil Jethani, Mukund Sudarshan, Ian Covert, Su-In Lee, and Rajesh Ranganath. Fastshap: Real-time shapley value estimation. *ArXiv*, abs/2107.07436, 2021. 1

[23] Neil Jethani, Mukund Sudarshan, Ian Connick Covert, Su-In Lee, and Rajesh Ranganath. FastSHAP: Real-Time Shapley Value Estimation. In *International Conference on Learning Representations*, 2022. 3

[24] Jinkyu Kim, Hyunggi Cho, Myung Hwangbo, Jae-hyung Choi, John Canny, and Youngwook Paul Kwon. Deep traffic light detection for self-driving cars from a large-scale dataset. In *2018 21st International Conference on Intelligent Transportation Systems (ITSC)*, pages 280–285, 2018. 1

[25] Jinkyu Kim, Anna Rohrbach, Zeynep Akata, Suhong Moon, Teruhisa Misu, Yi-Ting Chen, Trevor Darrell, and John Canny. Toward explainable and advisable model for self-driving cars. *Applied AI Letters*, 2(4):e56, 2021. 1

[26] Michihiro Kuroki and Toshihiko Yamasaki. Fast Explanation Using Shapley Value for Object Detection. *IEEE Access*, 12:31047–31054, 2024. 3, 7

[27] Anton Kuznetsov, Balint Gyevnar, Cheng Wang, Steven Peters, and Stefano V. Albrecht. Explainable ai for safe and trustworthy autonomous driving: A systematic review. *IEEE Transactions on Intelligent Transportation Systems*, 25(12):19342–19364, 2024. 3

[28] Mingfu Liang, Jong-Chyi Su, Samuel Schulter, Sparsh Garg, Shiyu Zhao, Ying Wu, and Manmohan Chandraker. Aide: An automatic data engine for object detection in autonomous driving. In *Proceedings of the IEEE/CVF Conference on Computer Vision and Pattern Recognition (CVPR)*, pages 14695–14706, 2024. 3

[29] Tsung-Yi Lin, Michael Maire, Serge J Belongie, Lubomir D Bourdev, Ross B Girshick, James Hays, Pietro Perona, Deva Ramanan, Piotr Dollár, and C Lawrence Zitnick. Microsoft COCO: Common Objects in Context. *CoRR*, abs/1405.0312, 2014. 7

[30] Scott M Lundberg and Su-In Lee. A Unified Approach to Interpreting Model Predictions. In *Advances in Neural Information Processing Systems*, pages 4768–4777. Curran Associates, Inc., 2017. 2

[31] Sina Mohseni, Mandar Pitale, Vasu Singh, and Zhangyang Wang. Practical solutions for machine learning safety in autonomous vehicles, 2019. 1

[32] Milad Moradi, Ke Yan, David Colwell, Matthias Samwald, and Rhona Asgari. Model-agnostic explainable artificial intelligence for object detection in image data. *Engineering Applications of Artificial Intelligence*, 137:109183, 2024. 1

[33] Tomasz Nowak, Michał R. Nowicki, Krzysztof Ćwian, and Piotr Skrzypczyński. How to improve object detection in a driver assistance system applying explainable deep learning. In *2019 IEEE Intelligent Vehicles Symposium (IV)*, pages 226–231, 2019. 1

[34] Deepan Chakravarthi Padmanabhan, Paul G. Plöger, Octavio Arriaga, and Matias Valdenegro-Toro. Dext: Detector explanation toolkit. In *Explainable Artificial Intelligence - First World Conference, xAI 2023, Lisbon, Portugal, July 26-28, 2023, Proceedings, Part II*, pages 433–456. Springer, 2023. 2

[35] Vitali Petsiuk, Abir Das, and Kate Saenko. RISE: randomized input sampling for explanation of black-box models. In *British Machine Vision Conference (BMVC)*. BMVA Press, 2018. 2

[36] Vitali Petsiuk, Rajiv Jain, Varun Manjunatha, Vlad I. Morariu, Ashutosh Mehra, Vicente Ordonez, and Kate Saenko. Black-box explanation of object detectors via saliency maps. In *2021 IEEE/CVF Conference on Computer Vision and Pattern Recognition (CVPR)*, pages 11438–11447, 2021. [2](#), [3](#)

[37] Joseph Redmon, Santosh Kumar Divvala, Ross B. Girshick, and Ali Farhadi. You only look once: Unified, real-time object detection. In *Proceedings of CVPR*, pages 779–788, 2016. [3](#)

[38] Shaoqing Ren, Kaiming He, Ross Girshick, and Jian Sun. Faster R-CNN: Towards Real-Time Object Detection with Region Proposal Networks. In *Advances in Neural Information Processing Systems*. Curran Associates, Inc., 2015. [3](#)

[39] Marco Tulio Ribeiro, Sameer Singh, and Carlos Guestrin. "Why should i trust you?" Explaining the predictions of any classifier. In *Proceedings of the ACM SIGKDD International Conference on Knowledge Discovery and Data Mining*, pages 1135–1144. Association for Computing Machinery, 2016. [2](#), [3](#)

[40] Stephan R. Richter, Zeeshan Hayder, and Vladlen Koltun. Playing for Benchmarks . In *2017 IEEE International Conference on Computer Vision (ICCV)*, pages 2232–2241, Los Alamitos, CA, USA, 2017. IEEE Computer Society. [7](#)

[41] Ramprasaath R. Selvaraju, Michael Cogswell, Abhishek Das, Ramakrishna Vedantam, Devi Parikh, and Dhruv Batra. Grad-CAM: Visual explanations from deep networks via gradient-based localization. In *International Conference on Computer Vision (ICCV)*, pages 618–626. IEEE, 2017. [2](#)

[42] Ashish Vaswani, Google Brain, Noam Shazeer, Niki Parmar, Jakob Uszkoreit, Llion Jones, Aidan N Gomez, Łukasz Kaiser, and Illia Polosukhin. Attention Is All You Need. In *Advances in Neural Information Processing Systems*, 2017. [3](#)

[43] Ao Wang, Hui Chen, Lihao Liu, Kai Chen, Zijia Lin, Jungong Han, and Guiguang Ding. YOLOv10: Real-Time End-to-End Object Detection, 2024. [3](#)

[44] Haofan Wang, Zifan Wang, Mengnan Du, Fan Yang, Zijian Zhang, Sirui Ding, Piotr Mardziel, and Xia Hu. Score-CAM: Score-Weighted Visual Explanations for Convolutional Neural Networks. In *IEEE/CVF Conference on Computer Vision and Pattern Recognition (CVPR)*, 2019. [8](#)

[45] Zhou Wang, A C Bovik, H R Sheikh, and E P Simoncelli. Image quality assessment: from error visibility to structural similarity. *IEEE Transactions on Image Processing*, 13(4):600–612, 2004. [8](#)

[46] Nicolai Wojke, Alex Bewley, and Dietrich Paulus. Simple online and realtime tracking with a deep association metric. In *2017 IEEE International Conference on Image Processing (ICIP)*, pages 3645–3649, 2017. [3](#)

[47] Fisher Yu, Haofeng Chen, Xin Wang, Wenqi Xian, Yingying Chen, Fangchen Liu, Vashisht Madhavan, and Trevor Darrell. Bdd100k: A diverse driving dataset for heterogeneous multitask learning. In *Proceedings of the IEEE/CVF Conference on Computer Vision and Pattern Recognition (CVPR)*, 2020. [7](#)

[48] Yifu Zhang, Peize Sun, Yi Jiang, Dongdong Yu, Fucheng Weng, Zehuan Yuan, Ping Luo, Wenyu Liu, and Xinggang Wang. ByteTrack: Multi-Object Tracking by Associating Every Detection Box. *Proceedings of the European Conference on Computer Vision (ECCV)*, 2022. [3](#)

[49] Yian Zhao, Wenyu Lv, Shangliang Xu, Jinman Wei, Guanzhong Wang, Qingqing Dang, Yi Liu, and Jie Chen. Detrs beat yolos on real-time object detection. In *Proceedings of the IEEE/CVF Conference on Computer Vision and Pattern Recognition*, pages 16965–16974, 2024. [3](#)